

The origin of organic emission in NGC 2071[★]

T.A. van Kempen¹, C. M^cCoey², S. Tisi², D. Johnstone^{3,4,5}, and M. Fich²

¹Leiden Observatory, Leiden University, Niels Bohrweg 2, 2333 CA, Leiden, the Netherlands
e-mail: kempen@strw.leidenuniv.nl

²Department of Physics and Astronomy, University of Waterloo, Waterloo, Ontario, N2L 3G1, Canada

³Joint Astronomy Centre, 660 North A'ohoku Place, University Park, Hilo, HI 96720, USA

⁴National Research Council Canada, Herzberg Institute of Astrophysics, 5071 West Saanich Rd, Victoria, BC, V9E 2E7, Canada

⁵Department of Physics & Astronomy, University of Victoria, Victoria, BC, V8P 1A1, Canada

Received Jan 1, 2014

ABSTRACT

Context. The physical origin behind organic emission lines in embedded low-mass star formation has been fiercely debated in the last two decades. A multitude of scenarios have been proposed, from a hot corino to PDRs on cavity walls to shock excitation.

Aims. The aim of this paper is to determine the location and the corresponding physical conditions of the gas responsible for organics emission lines. The outflows around the small protocluster NGC 2071 are an ideal testbed to differentiate between various scenarios.

Methods. Using Herschel-HIFI and the SubMillimeter Array, observations of CH₃OH, H₂CO and CH₃CN emission lines over a wide range of excitation energies were obtained. Comparisons to a grid of radiative transfer models provide constraints on the physical conditions. Comparison to H₂O line shape is able to trace gas-phase synthesis versus a sputtered origin.

Results. Emission of organics originates in three separate spots: the continuum sources IRS 1 ('B') and IRS 3 ('A') as well as a new outflow position ('F'). Densities are above 10⁷ cm⁻³ and temperatures between 100 to 200 K. CH₃OH emission observed with HIFI originates in all three regions and cannot be associated with a single region. Very little organic emission originates outside of these regions.

Conclusions. Although the three regions are small (<1,500 AU), gas-phase organics likely originate from sputtering of ices due to outflow activity. The derived high densities (>10⁷ cm⁻³) are likely a requirement for organic molecules to survive from being immediately destroyed by shock products after evaporation. The lack of spatially extended emission confirms that organic molecules cannot (re)form through gas-phase synthesis, as opposed to H₂O, which shows strong line wing emission. The lack of CH₃CN emission at 'F' is evidence for a different history of ice processing due to the absence of a protostar at that location and recent ice mantle evaporation.

Key words. stars: formation, submillimeter: ISM, stars:protostars, circumstellar matter

1. Introduction

Strong emission lines of hydrogenated carbon-bearing species are a common feature associated with the early stages of star formation. Embedded high-mass protostars possess a so-called 'hot core' component (Kurtz et al. 2000), from which large quantities of emission lines from organic molecules have been detected (e.g., Comito et al. 2005). This spherically symmetric region around the massive protostar is powered solely by luminosities from the just-ignited protostar and its accretion flow.

Similar emission features of organic compounds have been detected around low-mass protostars (van Dishoeck et al. 1995; Cazaux et al. 2003; Bottinelli et al. 2004a; Bisschop et al. 2008; Caux et al. 2011), including simple sugars (Jørgensen et al. 2012). Even though most emission lines of the organics clearly originate in the inner few hundred AU, their physical origin is

fiercely debated. In one scenario, emission originates in a spherically symmetric component around the protostar similar to the hot core, referred to as the 'hot corino' (Ceccarelli et al. 2007). In some sources the molecular emission does not coincide with the positions where the continuum peaks and the protostar is believed to be located (e.g., Chandler et al. 2005). Observed line shapes, in particular the line wings, do not support a spherical model. Furthermore, SED and envelope modelling of low-mass protostars show that although central warm regions are possible (Shirley et al. 2002), typical sizes and column densities of the protostellar envelope are much larger and higher than predicted. Other sources of energy are required to explain the observations.

Abundances of molecules such as methanol and formaldehyde (CH₃OH and H₂CO) are factors of ~30-100 higher in protostellar environments than in dark clouds (Takakuwa et al. 1998), where non-thermal desorption dominates (Öberg et al. 2009). From examination of the physical and chemical conditions, release of icy grain mantles must play a key role (van der Tak et al. 2000; Maret et al. 2005). It is poorly understood in which situations thermal desorption of water (H₂O) (Sandford & Allamandola 1993) is dominant, when grain-grain collisions that shatter ice mantles (Jones et al. 1996) are required, or when sputtering by energetic particles produced in shocks play a large role

[★] This paper uses *Herschel* observations. *Herschel* is an ESA space observatory with science instruments provided by European-led Principal Investigator consortia and with important participation from NASA. This paper also makes use of SMA observations. The Sub-millimeter Array is a joint project between the Smithsonian Astrophysical Observatory and the Academia Sinica Institute of Astronomy and Astrophysics and is funded by the Smithsonian Institution and the Academia Sinica.

(Flower & Pineau Des Forêts 2010). Whatever the role, CH_3OH is a pure grain mantle product.

Bottinelli et al. (2004b) and Bisschop et al. (2008) showed the importance of resolved interferometric observations of organic emission. By resolving components and their conditions, differences in the formation of organics can be uncovered. Abundances of some species cannot be produced by grain surface hydrogenation alone. A combination of grain surface reactions and gas phase formation and/or destruction is often required.

Shock desorption has been invoked to account for observed offsets of organic emission when visibly associated with outflowing material (e.g. Buckle & Fuller 2002). Shocks and their associated cavities also allow for additional energy injections not possible in spherical models. Warm gas on the surface of outflow cavity walls has been invoked to explain observed CO $J=6-5$ emission (Spaans et al. 1995; van Kempen et al. 2009). There is no reason why this cannot be a physical driver for emission of organics, following the relatively high gas temperature of this component (Visser et al. 2012). An important constraint to the conditions is the amount of CH_3OH destroyed, either through dissociative desorption during the sputtering or reactions with H in the shock. Recently, Suutarinen et al. (2014) found that comparison of CH_3OH with H_2O can probe the conditions of irradiated shocks.

Most likely, the various origins coexist. This is best shown by the ongoing work in intermediate mass protocluster OMC 2 FIRS 4 (Kama et al. 2010, 2013; López-Sepulcre et al. 2013). The small scales show more than 4 components, while the observed methanol emission cannot be tied to one component, even though > 100 lines have been detected. Multiple components and origins are required.

The tightly packed proto-cluster NGC 2071, located at 422 pc (Carrasco-González et al. 2012; van Kempen et al. 2012) produces one of the most powerful outflows within 500 pc (Scoville et al. 1986; Butner et al. 1990). In combination with the relatively low stellar masses of all three protostars and a cleaner environment, it is a better candidate to differentiate between outflow driven scenarios and hot-core like origins or quantify the relative contributions of both. It is rich in molecular emission (Johnstone et al. 2003), at times showing two gaussian components of different widths.

In this paper, we present new results using observations of emission lines of three organic compounds: methanol (CH_3OH), formaldehyde (H_2CO) and methyl cyanide (CH_3CN). These three organic compounds are commonly used as tracers for chemical activity in nearby star forming regions (e.g., Jørgensen et al. 2011; Kama et al. 2013). Observations are obtained with ESA Herschel Space Observatory (Pilbratt et al. 2010) using the Heterodyne Instrument for the Far-Infrared (HIFI) (de Graauw et al. 2010), and the Sub-millimeter Array (SMA). The aim of this paper is to determine the location, excitation and physical conditions of the region(s) responsible for the organic emission in NGC 2071 and differentiate between a hot corino scenario or one related to the outflowing gas. Section 2 presents the observations, and subsequent results are listed in section 3. The analysis is done in Section 4. The origin scenario is discussed in Section 5, with conclusions summarized in Section 6.

2. Observations

Spectral line observations of HIFI (de Graauw et al. 2010) and the SMA were inspected for methanol (CH_3OH), formaldehyde (H_2CO) and/or methyl cyanide (CH_3CN) emission lines. To aid the analysis into the conditions that set the chemistry the 987 and

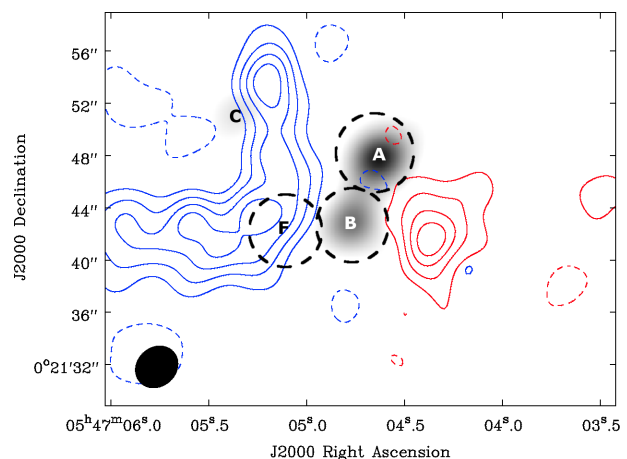


Fig. 1. Integrated line wings of ^{13}CO emission (blue and red) around NGC 2071 obtained with the SMA. It is overlotted on the 1.3 mm continuum emission (greyscale) in steps of 3, 6, 9, 12 σ (see van Kempen et al., 2012). Locations of continuum sources (A, B, and C) are labelled. The beam size of $3.4'' \times 2.9''$ is shown in a black ellipse in the lower left. Dashed circles indicate the regions integrated for organic emission, including region F (see text).

Table 1. Observational parameters.

HIFI					
Setting	Freq. ¹ GHz	Band	θ_{mb} ''	ObsId.	RMS ² mK
1	547.676	1a	38.0	1342194490	5
2	556.936	1a	38.0	1342205274	15
3	752.033	2b	28.0	1342194682	19
4	987.927	4a	21.5	1342204503	25
5	1095.67	4b	19.0	1342227395	17
6	1113.343	4b	19.0	1342194790	18
7	1153.127	5a	18.5	1342206128	93
SMA					
Bandwidth			2x4 GHz		
Center Frequencies			230.5 & 219.0 GHz		
Configuration			SMA Compact		
Beam size			3.4'' x 2.9''		
Observation Date			January 13th 2010		

¹ Center Frequency of the HIFI Band.

² Measured in 0.5 km s^{-1} bins.

752 GHz H_2O lines are included in this paper (Suutarinen et al. 2014).

SMA observations of the line wings of $^{13}\text{CO } J=2-1$ (see Fig. 1) are used as a reference for the location of the outflowing gas. Table 1 lists the observational settings of both the SMA and Herschel-HIFI observations. Data reduction was performed using a combination of the following software tools: the MIR package for IDL, MIRIAD, HIPE¹ (Ott 2010) and CLASS in GILDAS².

¹ HCSS/HSspot/HIPE is a joint development (are joint developments) by the Herschel Science Ground Segment Consortium, consisting of ESA, the NASA Herschel Science Center, and the HIFI, PACS and SPIRE consortia.

² GILDAS is a software package developed by IRAM to reduce and analyze astronomical data; <http://www.iram.fr/IRAMFR/GILDAS>.

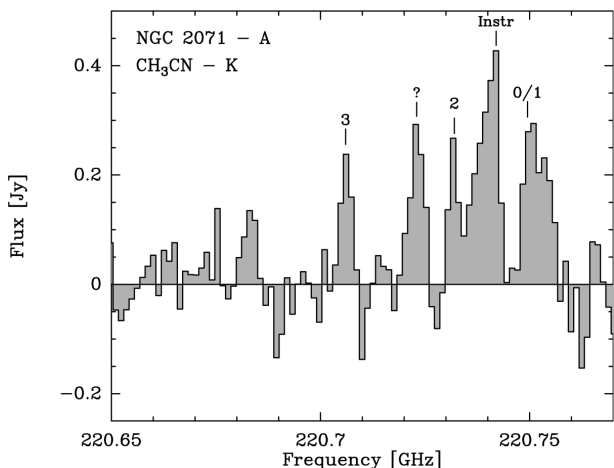


Fig. 2. CH₃CN $K = 12 - 11$ ladder between 220.65 and 220.8 GHz observed by the SMA at the position of region 'A'. The instrumental feature between the 2 and 0/1 blended transitions is labelled with "Instr".

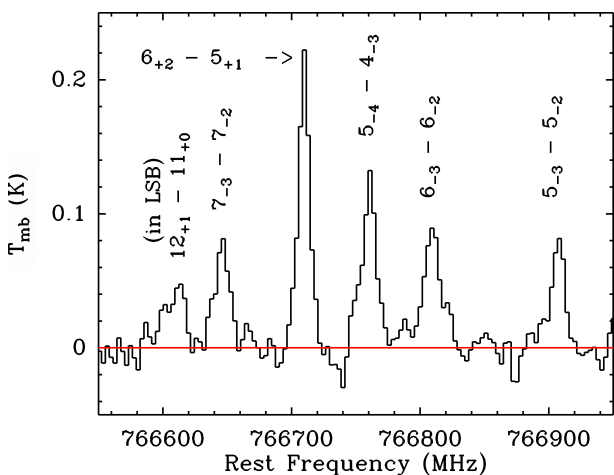


Fig. 3. Detected CH₃OH lines observed with HIFI in 400 MHz centered at 766.75 GHz. Note that the $12_{+1}-11_{+0}$ line is from the lower sideband, with a rest frequency of 751.55 GHz. Channels are resampled to a width of 0.75 km s^{-1} . The baseline is shown as a horizontal red line. At this frequency, the beam of HIFI is $26''$.

2.1. HIFI

HIFI³ observations of NGC 2071 were carried out within the scope of the WISH key program (van Dishoeck et al. 2011), targeting rotational emission of H₂O. All pointings were centered at a position with a Right Ascension of 05h47m04.4s and a Declination of 00d21m49s. Except the setting targeting the ground-state H₂O line at 557 GHz (setting 2), all observations were done

³ HIFI has been designed and built by a consortium of institutes and university departments from across Europe, Canada and the United States under the leadership of SRON Netherlands Institute for Space Research, Groningen, The Netherlands and with major contributions from Germany, France and the US. Consortium members are: Canada: CSA, U.Waterloo; France: CESR, LAB, LERMA, IRAM; Germany: KOSMA, MPIfR, MPS; Ireland, NUI Maynooth; Italy: ASI, IFSI-INAF, Osservatorio Astrofisico di Arcetri- INAF; Netherlands: SRON, TUD; Poland: CAMK, CBK; Spain: Observatorio Astronómico Nacional (IGN), Centro de Astrobiología (CSIC-INTA). Sweden: Chalmers University of Technology - MC2, RSS & GARD; Onsala Space Observatory; Swedish National Space Board, Stockholm University - Stockholm Observatory; Switzerland: ETH Zurich, FHNW; USA: Caltech, JPL, NHSC.

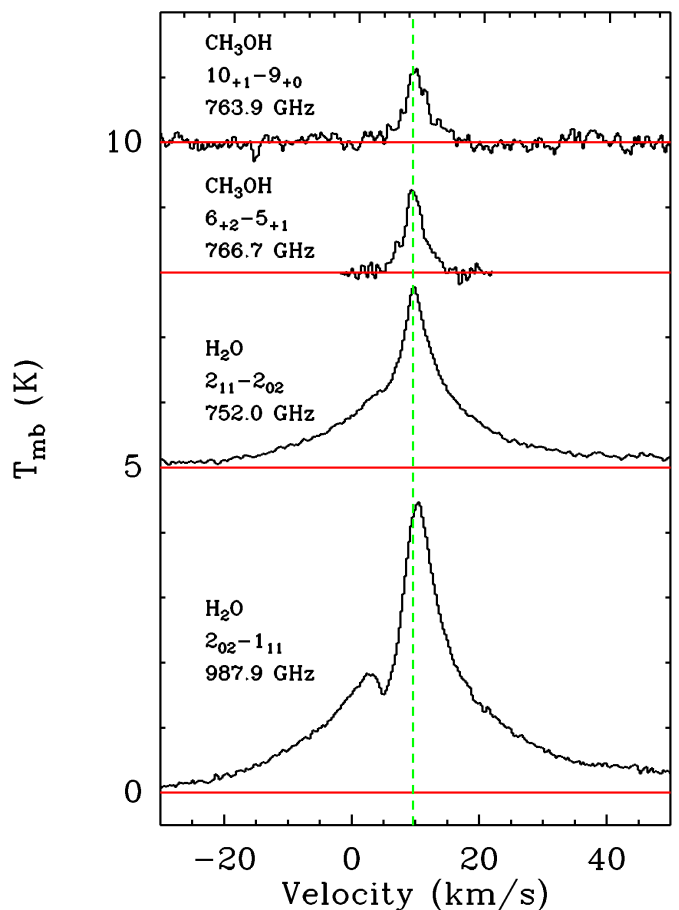


Fig. 4. HIFI Line profiles of the CH₃OH $10_{+1}-9_{+0}$ (763.9 GHz) and $6_{+2}-5_{+1}$ (766.7 GHz) and H₂O $2_{11}-2_{02}$ (752.0 GHz) and $2_{02}-1_{11}$ (987.9 GHz) transitions. The CH₃OH lines are multiplied by a factor 5. Spectra are binned to 0.3 km s^{-1} bins. Respective baselines are shown in red. The V_{LSR} of NGC 2071 is shown in green. Note that the wings of the H₂O lines extent beyond the horizontal scale.

using DBS Fast Chop modes (See Table 1 for the observed HIFI bands and Observations Identification Numbers). After delivery, data were reprocessed with the default pipeline in HIPE 7.1 (Ott 2010) and calibration version HIFI_CAL_6_0. Further data reduction was done using HIPE 8.1. H and V spectra were averaged together prior to converting the data to the velocity scale. The WBS spectrometer provided a 4 GHz bandwidth with a 1.1 MHz frequency resolution (0.7 to 0.4 km s^{-1}). The beam of HIFI ranges from 18 to $41''$ much larger than the structure seen in van Kempen et al. (2012) (see Table 1 and Fig. 1). Relative calibration errors are 15% for all bands except the one in Band 5, which is 20%.

2.2. SMA

The Sub-millimeter Array (SMA) observed NGC 2071 in compact configuration on January 3rd 2010 using a bandwidth of 4 GHz centered at 230.538 GHz and 4 GHz centered at 219.634 GHz and a spectral resolution of 0.3 km s^{-1} . The phase center was located at a Right Ascension of 05h47m04.7s and a Declination of +00d21m44.0s, the same coordinates used to carry

⁴ The calibrated data is available through the Radio Telescope Data Center hosted by the Smithsonian Astrophysical Observatory (<http://www.cfa.harvard.edu/rtdc/>)

Table 2. Emission lines detected with HIFI. The average uncertainty on the integrated intensity is estimated at 15% (see text)

Transition	Type	Freq. [GHz]	E_{up} [K]	$\int T_{\text{MB}}dV$ [K km s ⁻¹]
CH ₃ OH				
3 ₋₃ - 3 ₋₂	E	766.98	76.64	1.03
4 ₋₃ - 4 ₋₂	E	766.96	85.92	1.03
6 ₊₂ - 5 ₊₁	A	766.71	86.46	0.90
5 ₋₃ - 5 ₋₂	E	766.91	97.53	0.41
8 ₊₀ - 7 ₊₁	E	543.08	96.61	0.75
6 ₋₃ - 6 ₋₂	E	766.81	111.46	0.56
5 ₋₄ - 4 ₋₃	E	766.76	122.72	0.66
7 ₋₃ - 7 ₋₂	E	766.65	127.71	0.39
10 ₊₁ - 9 ₊₀	A	763.95	141.08	1.19
7 ₊₄ - 6 ₊₃	A	974.87	145.33	0.88
8 ₋₃ - 8 ₋₂	E	766.40	146.28	0.33
10 ₊₂ - 9 ₊₁	A	986.10	165.40	0.38
9 ₋₃ - 9 ₋₂	A	766.08	167.16	<0.30
11 ₊₁ - 10 ₊₁	A	536.19	169.01	0.50
11 ₊₂ - 10 ₊₁	E	558.34	175.15	0.40
10 ₋₃ - 10 ₋₂	E	765.51	190.37	0.29
12 ₊₁ - 11 ₊₀	E	751.55	202.12	0.27
11 ₋₃ - 11 ₋₂	E	764.81	215.90	0.26
12 ₊₃ - 11 ₊₂	E	1109.58	228.78	0.33
15 ₊₂ - 14 ₊₁	E	754.22	300.98	0.36
18 ₊₁ - 17 ₊₀	A	1105.94	407.62	0.23
23 ₊₁ - 22 ₋₂	A	977.37	427.10	0.24
20 ₊₀ - 19 ₋₁	A	1095.06	497.93	0.23
H ₂ O				
2 ₀₂ -1 ₁₁	Para	987.927	100.8	88.48
2 ₁₁ -2 ₀₂	Para	752.033	136.9	46.62

out the HIFI observations. Continuum results were published in van Kempen et al. (2012). With a spatial resolution corresponding to ~ 1300 AU ($3.4'' \times 2.9''$), the full extent of the flow is spatially resolved, as are the separations between most of the individual protostars (van Kempen et al. 2012). The noise levels were 4 mJy beam⁻¹ for the continuum and 0.08 Jy beam⁻¹ per 0.8 km s⁻¹ bin. This corresponds to ~ 0.4 K in the 0.8 km s⁻¹ bins. Calibration uncertainty in the lines was derived to be 15% after the model fitting of Uranus. We will follow the notation from van Kempen et al. (2012), in which the source IRS 3 is labelled as 'A', IRS 1 as 'B' and IRS 5 as 'C'. Note that the phase center is located in between 'A' and 'B'. Due to the placement of correlator chunks, which optimized coverage for the CO isotopologues and continuum, several instrumental artifacts needed to be flagged at semi-regular intervals. The only one affecting emission lines of H₂CO, CH₃OH or CH₃CN appears between the $K = 1$ and 2 transitions of the $J = 12-11$ ladder of CH₃CN. The artificial feature is 8 channels wide with a regular increase per channel. Spectra were corrected by fitting and subtracting a step-function to these channels. Figure 2 presents the uncorrected CH₃CN spectrum for source 'A'.

3. Results

3.1. HIFI

In the HIFI bands, a total of 24 CH₃OH emission lines were identified, but no CH₃CN or H₂CO lines were seen. The H₂O

lines are both very clearly detected with very broad line wings (>20 km s⁻¹, see Fig. 4). The rms noise levels can be found in Table 1. More details on water emission will be in a forthcoming paper (M^cCoe & van Kempen, in prep). Quantum numbers, rest frequencies, energy levels and velocity integrated flux densities of the detected transitions are listed in Table 2. Note that no lines were found in Band 5, which has a higher calibration uncertainty than the other Bands. As such the uncertainty for all lines in Table 2 is assumed to be 15%. Rest frequencies of all detections were checked against the molecular line survey of Kama et al. (2013). One feature was removed as questionable. Energy levels range from 75 to 500 Kelvin. The bulk of the lines are observed around frequencies of 766 GHz, within the K_{up} to $K_1 = -3$ to -2 ladder (See Fig. 3). All detected lines have $K_{\text{up}} = \leq |3|$. Lines are consistently ≈ 6 km s⁻¹ wide. No evidence was found for an increase of line width as a function of energy level, as suggested by Kama et al. (2010). A very small shift in velocity with respect to the source velocity is at times observed, but this is more likely to be an artifact of the methanol lines not being in the center of the HIFI bandpass and not a physical effect.

3.2. SMA

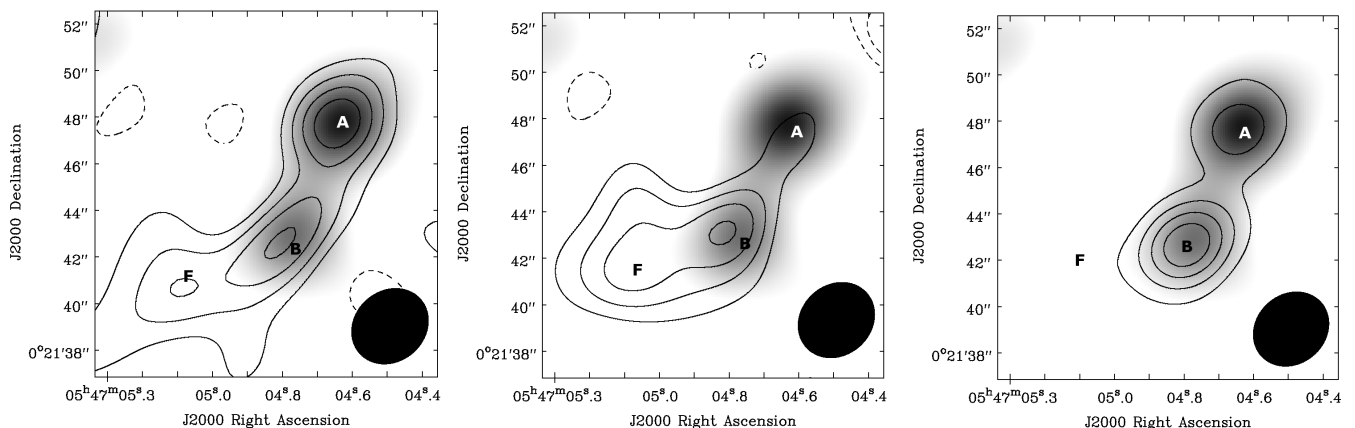
Table 3 lists the detected CH₃OH, H₂CO and CH₃CN transitions with quantum numbers, rest frequencies, energy levels and integrated flux densities. For CH₃OH, only transitions with $K_{\text{up}} \leq |2|$ are seen, with one line $K_{\text{up}} = 0$. For CH₃CN, all detections are part of the $K=12-11$ ladder around 220.7 GHz. All detected lines have line widths ranging between 5.9 to 8.0 km s⁻¹ wide, similar to the line widths of CH₃OH detected by HIFI. Emission is spatially resolved into three positions for most lines (see Fig. 5). Integrated flux densities are given for the three positions, labelled 'A', 'B' and 'F'. The 'F' position is a position $4''$ west of B, with no continuum nor infra-red emission peak (van Kempen et al. 2012). Figure 1 shows 'F' to be a position associated with entrained material. No velocity shifts were found between the three different positions.

The observed spatial distributions were fitted with Gaussian profiles with the goal to determine whether or not emission was spatially resolved. Spatial scales $>1.5 \times$ the beam size along at least one axis were required. It was found that only H₂CO emission from 'F' and 'B' is clearly spatially resolved. It is unresolved for 'A'. CH₃OH emission is predominantly unresolved at all three positions for all transitions. Only the CH₃OH transition at 218.44 GHz hints at resolved emission at 'F', albeit only marginally ($\sim 1.2 \times$ the beam). All CH₃CN emission is unresolved at positions 'A' and 'B' and undetected at 'F'. Note that SMA observations resolve out any structure larger than $13''$ (van Kempen et al. 2012). The narrow H₂CO component seen in Johnstone et al. (2003) between 2.2 and 2.9 km s⁻¹, is not detected and assumed to be resolved out. It thus originates within a component that is smoothly distributed on scales of $\sim 4,000$ AU or larger.

After correcting for the difference in beam size, the sum of the three regions seen in the H₂CO $3_{03}-2_{02}$ transition reproduces 96% of the emission listed in Johnstone et al. (2003). For the H₂CO $3_{22}-2_{21}$ transition, the 16 km s⁻¹ wide component is not detected by the SMA. The sum of the three regions equals to 75% of the total intensity reported in Johnstone et al. (2003). It should be noted that the wide velocity component seen in Johnstone et al. (2003) was solely detected in the H₂CO $3_{22}-2_{21}$ transition, and not in any other line included in their study. For the 4_2-3_1 line at 218.44 GHz, the three regions reproduce 91% of

Table 3. Detected CH_3OH , CH_3CN and H_2CO with the SMA. Lines are integrated over their width and converted to Kelvin km s^{-1} . Uncertainty of the flux density on all lines is 15%

Molecule	Transition	Type	Frequency [GHz]	E_{up} [K]	$\int T_{\text{MB}} dV$ [K km s^{-1}]		
					A	B	F
CH_3OH	$3_{-2} - 4_{-1}$	E	230.03	39.8	3.7	12.7	5.4
	$4_{+2} - 3_{+1}$	E	218.44	45.5	5.7	37.1	50.5
	$8_{-1} - 7_0$	E	229.76	89.1	48.4	64.2	76.7
	$8_{+0} - 7_{+1}$	E	220.08	96.6	4.6	24.2	14.9
	$10_{+2} - 9_{+3}$	A	231.28	110.9	8.2	14.0	-
	$10_{+2} - 9_{+3}$	A	231.42	110.9	19.4	11.3	8.5
H_2CO	$3_{0,3} - 2_{0,2}$	para	218.22	21.0	213	267.0	184.0
	$3_{2,2} - 2_{2,1}$	para	218.48	68.1	90.8	108.8	56.4
	$3_{2,1} - 2_{2,0}$	para	218.76	68.1	93.1	103.0	53.9
CH_3CN	0/1		220.75	68.9	48.3	62.4	-
	2		220.73	97.4	45.9	72.6	-
$J =$	3		220.71	133.2	26.0	34.2	-
12-11	4		220.68	183.1	20.1	21.7	-
ladder	5		220.64	247.4	-	14.1	-
	6		220.59	325.9	-	13.2	-

**Fig. 5.** H_2CO 218.48 GHz (*left*), CH_3OH 218.44 GHz (*middle*) and CH_3CN 220.71 GHz (*right*) maps, revealing that the emission originates from the 'A' and 'B' cores and the blue flow (marked A, B and F). Contours are overplotted on the continuum emission from van Kempen et al. (2012) in 20, 40, 60 and 80% of the peak line integrated intensity, which is always located at core B.

the observed JCMT emission. Given the uncertainties in absolute flux calibration of both the JCMT (20%) and SMA (15%), organic emission seen with the JCMT is almost fully recovered by the SMA by summing the emission of the three regions. We thus assume that for all lines detected by the SMA, emission is produced in these three regions and not in any undetected component resolved out, or other regions within the JCMT beam.

4. Analysis

4.1. Excitation of CH_3OH and H_2CO

Most CH_3OH and CH_3CN transitions inherently possess high critical densities (10^9 cm^{-3} or higher, see Johnstone et al. 2003). As such, excitation conditions can reliably be derived using the 1-D non-LTE radiative transfer code RADEX (van der Tak et al. 2007) from line ratios. The transitions are assumed to be completely optically thin and fill the beam, following Kama et al. (2010). Optical depth effects and other radiative transfer effects such as IR pumping are discussed later.

A large grid of RADEX models was run to derive E-type CH_3OH , H_2CO and CH_3CN emission line predictions between 215 and 1115 GHz, using datafiles provided by LAMDA⁵ (Schöier et al. 2005) with the upward rate coefficients calculated at the appropriate temperature. Temperatures ranged from 50 to 500 Kelvin, while densities were varied between 10^4 cm^{-3} and 10^9 cm^{-3} .

Most collisional rate coefficient are limited to $J_{\text{up}} = 15$ and temperatures of 200 K. At higher kinetic temperatures, downward collisional rate coefficients of 200 K are used. The RADEX line width was set to 6 km s^{-1} . A column density of only 10^7 cm^{-2} was chosen, since we are interested in line ratios of optically thin transitions. Differential beam dilution is corrected using the method described in the appendix of B of (Tafalla et al. 2010) assuming the regions are point sources. Dilution factors are thus proportional to θ_{MB}^{-2} . However, test using the one-dimensional source structure (θ_{MB}^{-1}) show little to no changes.

⁵ the Leiden Atomic and Molecular Database: See <http://www.strw.leidenuniv.nl/~moldata/>

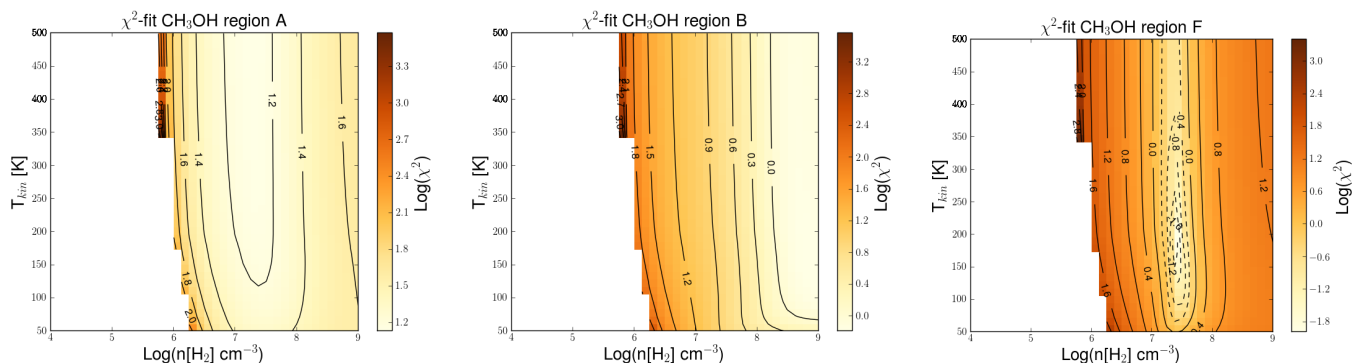


Fig. 6. Pearson's χ^2 results of line ratios predicted by RADEX modelling and the observed ratio for all detected E-type CH_3OH lines of the three regions (*Left*:A, *Middle*:B, *Right*:F). The color-scales are chosen such that lighter color indicates lower χ^2 values and better agreement with observed line ratio and models. Densities are well fitted with values of $2 \times 10^7 \text{ cm}^{-3}$ for region 'A', $> 3 \times 10^8 \text{ cm}^{-3}$ for region 'B' and $4 \times 10^7 \text{ cm}^{-3}$ for region 'F',

Predictions of line ratios were compared to the observed ratios of the five E-type CH_3OH lines detected with the SMA for each region. Figure 6 shows the results of a Pearson's χ^2 test⁶. The errors on individual ratios are 21%. The ratios reveal clear differences in the physical conditions between the regions, presented in Fig. 6. The best fit found for region 'F' is a density of $4 \pm 0.1 \times 10^7 \text{ cm}^{-3}$. Region 'A' is constrained to a density of $2 \pm 0.8 \times 10^7 \text{ cm}^{-3}$, while region 'B' is constrained to densities $> 2 \times 10^8 \text{ cm}^{-3}$. Temperatures are loosely constrained to values > 100 Kelvin.

Better constraints on the kinetic temperature can be obtained through comparison of the line ratio of H_2CO $3_{0,3}-2_{0,2}$ over $3_{2,2}-2_{2,1}$ with the RADEX model. Figure 7 shows the resulting line ratios of our RADEX grid of these two H_2CO lines. The observed ratios of the three regions are plotted at the densities derived using the χ^2 tests of the CH_3OH ratios. This results in temperature constraints of 215^{+200}_{-70} K for region 'A', 150^{+280}_{-50} K for region 'B' and 100^{+40}_{-15} K for region 'F'. The error bar on the temperature can be significant, especially for regions 'A' and 'B'. Much higher temperatures (> 400 K) are within uncertainty. This is in part due to the lack of collision rate coefficients above 300 K for H_2CO . However, constraints on lower temperatures are much better. Even with these large error, all three regions are warmer than the surrounding envelope, but not hot ($T > 500$ K). Due to the molecular structure of H_2CO , there is no difference between using the $3_{2,2}-2_{2,1}$ or $3_{2,1}-2_{2,0}$ transition. Given the near identical line ratios of either with respect to the $3_{0,3}-2_{0,2}$ line, the temperature constraint can be assumed to be robust and not affected by observational biases.

The narrow range of constraints for 'F' imply that the emission in that region comes from a more homogeneous medium than 'A' or 'B'. The less restrictive fits in density around the protostellar positions 'A' and 'B' likely indicate density gradients within the emitting region. The significant differences in density ($2 \times 10^7 \text{ cm}^{-3}$ vs. $3 \times 10^8 \text{ cm}^{-3}$) and, to a lesser extent, temperature (215 K vs. 150 K) between 'A' and 'B' are surprising given the lack of difference in line width (6 km s^{-1} for both), individual line emission of the H_2CO $3_{2,2}-2_{2,1}$ line (109 vs 91 K km s^{-1}), $3_{0,3}-2_{0,2}$ line (267 vs 213 K km s^{-1}), resolved dust emission (0.13 Jy beam^{-1} vs. 0.12 Jy beam^{-1} , see Table 3 and Fig. 2 in van Kempen et al. 2012) or stellar ($0.9 M_\odot$ vs. 0.5

M_\odot) and individual envelope masses (8.2 M_\odot vs. 14.2 M_\odot). The main difference between the two regions is that 'B' powers the large NGC 2071 outflow, while 'A' possesses a much weaker flow (Carrasco-González et al. 2012).

4.2. Optical depth

The assumption that the observed methanol lines are all optically thin must be investigated further. Using RADEX one can determine the column densities and in turn the associated optical depths. It should be noted that the solution is degenerate with an assumed source size within a single beam. Smaller source sizes require higher column densities and thus higher optical depths are to reproduce the same amount of emission. If the source fills the SMA beam, as assumed above, a column of $4 \times 10^{15} \text{ cm}^{-2}$ was derived to best fit the observed flux densities. In this model, optical depths are typically 0.01 or lower. RADEX shows that to produce optically thick lines with the observed emission, a column of $8 \times 10^{17} \text{ cm}^{-2}$ or higher is required. Such a column corresponds to a source size 14 times smaller than the SMA beam, equal to ~ 90 AU.

However, at these high column densities, some lines will maser, affecting line ratios. The 218.44 GHz line is a weak maser, but shows similar line strengths when masing. The largest effect is seen for the ratios between the 218.44, 220.08 and 229.76 GHz lines. At higher columns, RADEX shows the 229.76 line as an absorption feature of similar depth as the emission of the 218.44 GHz line. However, no absorption was seen. In addition, the 220.08 line should be 100 times brighter than the 218.44 GHz line, while a ratio of about 0.5 to 2.5 was observed. From this, we can thus exclude that the emission originates from a very small region with a very high column density. The theoretically largest column that correctly reproduces the observed line ratios is a few times 10^{16} cm^{-2} , corresponding to an optical depth (τ) of 0.4. The assumption that all CH_3OH emission is optically thin is thus justified.

Besides a high optical depth, IR pumping of low density (10^3 cm^{-3}) methanol gas could also influence the observed line ratios for $v=0$ rotationally excited transitions (Leurini et al. 2007). Observations of torsionally excited methanol lines ($v=1$) are typically invoked to break the degeneracy. Although over 6 torsionally excited transitions were covered in the bandpass of the SMA, none were detected for the achieved sensitivity of (71 mJy in 2 km s^{-1} bins). In addition, no $v=1$ transitions were detected

⁶ Pearson's test is defined as $\chi^2 = \sum_{i=1}^n \frac{(R_i - P_i)^2}{P_i}$ with R_i the observed ratio and P_i the calculated ratio over a total of n ratios, in which the smallest χ^2 gives the best fit.

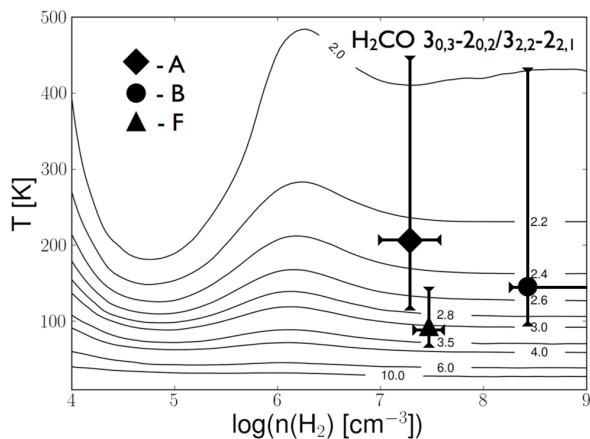


Fig. 7. Line ratio of H₂CO 3_{0,3}-2_{0,2} over 3_{2,2}-2_{2,1} modelled with RADEX. Observed line ratios are shown with a diamond (A), circle (B) and triangle (F) at the best-fit densities derived using the CH₃OH line ratios (see text). Error bars for the uncertainties originate from the line ratio error (21%). Errors on the densities originate from the χ^2 fitting. Temperatures are 215 K (A), 150 K (B) and 100 K (F).

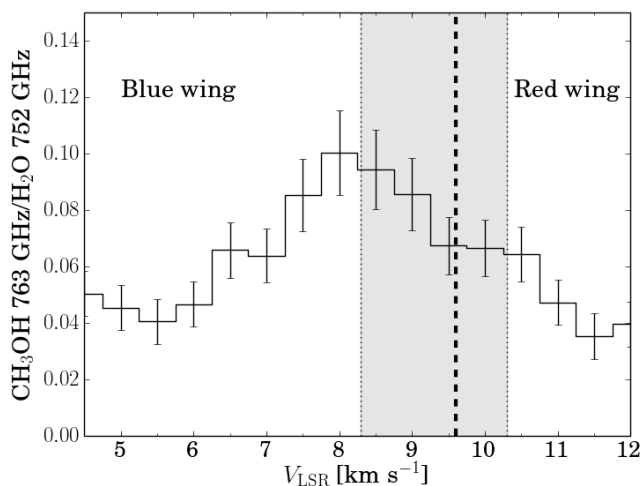


Fig. 8. Line ratio of the CH₃OH 10₊₁-9₊₀ over the H₂O 2₁₁-2₀₂ transitions, both rebinned to 0.5 km s⁻¹. The V_{LSR} is shown with a dashed line. The range of velocities where the high optical depth of the water line is hypothesized to affect the derived ratio is shown in grey. No correction has been applied (see text).

in the HIFI bandpass. This indicates IR pumping has little to no effect on the methanol emission. RADEX experiments with a grey body radiation field and lower densities showed that although the ratios of non-masing lines are indeed reproduced, it is impossible to simultaneously quench all three maser lines and produce the correct ratios. It is possible to add a very small (<50 AU) IR pumped component to the observed ratios. This can account for 25% of the observed line strengths. Whether or not such a component is present requires deep observations of the $\nu=1$ transitions, e.g. using the band around 241.2 GHz.

4.3. Excitation of CH₃CN

RADEX results for CH₃CN line ratios cannot improve on the solutions for the physical conditions obtained with H₂CO and CH₃OH, as all detected lines are part of the $J=12-11$ ladder.

From the RADEX models we derive a kinetic temperature of 200 K or higher for 'A' and ~ 150 K for 'B'. These values are consistent with the results of CH₃OH and H₂CO. It is thus reasonable to assume that the CH₃CN emission originates from the same gas as CH₃OH and H₂CO in 'A' and 'B'. However, CH₃CN emission is absent from 'F'.

With the optically thin assumption, the similarity of line ratios between CH₃CN, H₂CO and CH₃OH in 'A' and 'B', and the observed strength of the emission of H₂CO and CH₃OH in 'F', the relative abundance of CH₃CN w.r.t. H₂CO and CH₃OH must be almost two orders of magnitude lower at 'F' than in 'A' and 'B'. Excitation conditions cannot explain the lack of CH₃CN emission at 'F'.

4.4. Velocity profile: comparison to H₂O

The behaviour of the observed line ratio between CH₃OH and H₂O emission lines away from the source velocity differentiates between two potential formation routes of H₂O (Suutarinen et al. 2014). If gas-phase CH₃OH and H₂O are created solely through grain mantle evaporation, the ratio will be flat. However, if gas-phase synthesis of H₂O is taking place, the ratio will drop as more H₂O is created from shocked material. A significant optical depth in the water line causes observed ratios to be higher than physical processes would produce. Although an optical depth cannot be derived due to a lack of observed isotopologues, it is hypothesized that the H₂O 752 GHz may be affected near the line center (between 8.3 to 10.3 km s⁻¹). In outflows of low-mass protostars (e.g., Kristensen et al. 2010), optical depth are factors of a few at line center.

However, due to the high critical density of water transitions ($>10^8$ cm⁻³ for both the 987 and 752 GHz line), the assumed optically thick emission is most often effectively thin. The effects of water opacity on the ratio are still relatively small. See e.g., Fig. 3 of Suutarinen et al. (2014). For velocities where optical depth may play a role, the ratio is overestimated by a factor 2 at most.

Figure 8 shows the ratio of 763 10₁-9₀ CH₃OH transition and the 752 2₁₁-2₀₂ H₂O line. The observed CH₃OH/H₂O ratio clearly drops as a function of velocity on the blue wing. The red wing also is falling, although the number of channels not affected by optical depth is marginal. Velocities between 8.5 and 10.2 km s⁻¹ are thought to be affected by optical depth. As seen in the lower excited 987 GHz H₂O line, optical depth is expected to be at its highest there causing the ratios at these velocities to be higher.

Line ratios of other CH₃OH/H₂O combinations (e.g., the group of methanol lines at 766 GHz) show near identical profiles: A clear drop in the ratio on the blue side in combination with a drop on the red side and a middle likely affected by optical depth. Ratios derived using the 987 GHz H₂O line are more affected by optical depth, but still reproduce the falling ratio of the blue wing.

5. Discussion: Origin of organic emission.

Using the optically thin approximation, the observed spatial separation between the regions and lack of large-scale CH₃OH emission, CH₃OH HIFI detection originate solely in the three regions. The detected flux density for each line is a simple sum:

$$CH_3OH = C * (X_A * R_A + X_B * R_B + X_F * R_F) \quad (1)$$

CH₃OH is the total observed emission within the HIFI beam. R_X is the predicted emission from RADEX of region 'A', 'B' or 'F'

for that transition, and X the relative contribution. C is a constant to ensure the sum equals observed intensities.

If it is assumed X_A , X_B and X_F do not vary for individual CH_3OH lines, and are thus not vectors themselves, the set of equations can be solved by rewriting the equation for individual CH_3OH line contributions into a vector notation covering all the HIFI CH_3OH lines.

$$\overrightarrow{CH_3OH} = \vec{C} * (X_A * \vec{R}_A + X_B * \vec{R}_B + X_F * \vec{R}_F) \quad (2)$$

$\overrightarrow{CH_3OH}$ is a vector, one column wide, containing the HIFI-detected emission line flux densities. \vec{R}_X are the vectors, again one column wide, containing the predicted fluxes obtained from RADEX for the 14 HIFI E-Type methanol transitions with $J \leq 15$. Higher J transitions are not available in the molecular datafile. A-Type methanol is not included, since no constraints from the SMA are given for A-Type methanol transitions. Even assuming they originate under identical conditions with an abundance ratio of 1:1, inclusion of A-Type methanol does not contribute to the analysis below. \vec{C} is the vector containing the constant C for each transition. Under the assumption that the source size is the same for all transitions, \vec{C} will depend on the model parameters. Its only dependency is on the frequency of the transition. This known quantity determines the beam dilution in the HIFI beam. We realize that Eq. 2 is an oversimplification, as X_A , X_B and X_F may vary from transition to transition. Similarly, source sizes may become smaller for higher excited transitions. However, given the uncertainties in the observed emission, these simplifications produce acceptable results.

Solving Eq. 2 using a least squares method, optimal values of 13% for X_A , 71% for X_B and 16% for X_F are derived. With constant calibration uncertainties (in the case for Herschel a conservative value of 10% on the flux densities is assumed), the square of the error on the relative contributions equals the mean error times the rank of the matrix divided by the number of transitions⁷. The solution actually has a rank of only 2 (as opposed to 3 as was expected). The reason for this reduction in rank is that emission contributions in the conditions for 'F' and 'B' are very similar for the transitions probed. These produce similar ladders and none of the transitions used can distinguish them. The statistical error on the values of 13, 71 and 16 % is 4%.

For the detected SMA transitions, the mean of the individual relative contributions is indeed close to this value. Relative contributions of some of the individual transitions also adhere to the relation. For example, the CH_3OH $3_{-2}-4_{-1}$ line in Table 3, 'A' contributes 17%, 'B' contributes 58% and 'F' contributes 25%. However, clear variation are visible. Stronger contributions from 'F' are detected for some transitions. Whether or not these are introduced by optical depths effects due to the beam at 'B', or if the inferred density gradient at 'B' comes into play, remains to be seen.

Tests using other density and temperature parameters for regions 'A' and 'B' (i.e., higher temperatures and densities) also show variations at the level of 5% in the inferred contributions.

Deviations in relative contributions for higher excitation lines were subsequently investigated. Changes larger than 20% in relative contributions to higher excitation lines (e.g. by forcing 'A' to contribute 50% of the observed emission of a CH_3OH line with $E_{\text{up}} = 400$ K) become very problematic. In such cases, HIFI detections with $E_{\text{up}} < 250$ K significantly violate the constraints set by the SMA detections. Variations of 5-10% are likely from

⁷ The error σ is calculated from $\sigma^2 = \sigma_f^2 * M/N$ with σ_f the mean flux density error, M the rank of the matrix and N the number of entries.

transition to transition. In addition, emission from 'B' and 'F' cannot be disentangled from Herschel transitions alone. The percentages of 'B' and 'F' originate from the best solution in the least squares fitting and the mean of the SMA emission quantities.

The absence of molecular data beyond a $J = 15$ likely hinders further interpretation. To improve on this analysis, a full radiative transfer model with power law exponents describing envelope structures is warranted. This is considered to be beyond the scope of this paper.

In the end, the emission contribution from each region to all HIFI detections are estimated to be :

- 15-20% originates in region 'A'
- 60-70% in region 'B'
- 15-25% in region 'F'.

In region 'F', it is clear that the emission is related to the outflowing gas in position, but not in velocity. The absence of any stellar source rules out any possibility of disk-related scenarios or a hot corino. Whether or not the emission from 'A' and 'B' are related to the outflow or are part of a hot corino is debatable. However, a case in which the outflow plays a strong role is more likely.

Typical spherical envelope models with power-law density profiles show the derived higher densities of a few times 10^7 cm^{-3} to a few times 10^8 cm^{-3} to be located on scales of ≈ 100 AU. Gas temperatures of 150-200 K are located at scales of 50 AU or less, very close to the inner edge of the model (Shirley et al. 2002; Jørgensen et al. 2002; Kristensen et al. 2012). Envelopes around the individual NGC 2071 sources have been found to be very similar to these typical low-mass protostellar envelopes (van Kempen et al. 2012).

A scenario in which organics formed within the icy grain mantles, were subsequently liberated by either sputtering or grain-grain collisions and are currently emitting in a compressed, UV heated gas component is much more likely. Recently, Kristensen et al. (2013) found kinematic components in H_2O resolved lines consistent with dissociative jet shocks in the inner 100 AU to explain distinct velocity components in H_2O spectra. Such components produce emission offset from the central velocity and as such cannot originate in a hot-core like environment. They are too powerful to be associated with potential non-dissociative shocks along the outflow cavity wall. An irradiated shock was inferred from the low abundances in that component.

Outflows are known to be present at the smallest scales: 'B' is known to be the launching point of the large scale bipolar jet of NGC 2071 (Skinner et al. 2009). 'A' is a source of strong water masers. The maser spots display significant velocity shifts, indicative of jet activity (Torrelles et al. 1998; Carrasco-González et al. 2012).

5.1. Evidence for CH_3OH destruction and H_2O gas-phase synthesis

The decreasing ratio of the line profiles (see Fig. 8) shows that the chemistry in NGC 2071 is likely similar as that found for NGC 1333 IRAS 4A and 4B (Suutarinen et al. 2014). Atomic hydrogen formed in the shock is able to destroy CH_3OH through chemical reactions featuring hydrogen extraction, e.g. $\text{H} + \text{CH}_3\text{OH} \rightarrow \text{H}_2 + \text{CH}_2\text{OH}$ or $\text{H} + \text{CH}_3\text{OH} \rightarrow \text{H}_2 + \text{CH}_3\text{O}$ (Baulch 2005). Both products are also quickly destroyed. All these reactions have activation energies of ~ 800 K, much lower

than similar reactions capable of destroying H₂O (activation energy of $\sim 10^4$ K). Gas-phase synthesis of H₂O apparently can take place along the entire flow, given the brightness of the lines. Methanol emission is constrained to regions 'A', 'B' and 'F' by local physical conditions. Only regions of sufficient density (10^7 cm⁻³) can shield methanol from the high-temperature gas and subsequent dissociation. The high spatial resolution observations (Fig. 5) show that the regions where these physical conditions occur are small (<1500 AU in size). Observationally, we can conclude that the most likely location of these regions is in the neighborhood of protostars. This is not surprising considering envelope densities. However, correct conditions can also occur elsewhere, with no protostar nearby (region 'F').

5.2. Evidence for ice processing of CH₃CN

The main difference between CH₃CN and CH₃OH is its formation. Both form predominantly on grain surfaces, but their reactions proceed differently under cold conditions. CH₃CN is mainly formed through CN reacting with CO and other carbon containing species, while CH₃OH is a hydrogenation product of CO. At low temperatures, hydrogen moves freely. However, due to the low mobility of CN, CH₃CN formation requires heating and/or irradiation. Garrod et al. (2008) show an increase of more than order of magnitude in both gas and ice abundances for CH₃CN as a function of time in various warm-up scenarios, while the CH₃OH or H₂CO formation remains unaltered compared to the cold phase formation. Additional gas-phase formation routes for CH₃CN after grain mantle evaporation cannot be invoked, as these typically produce abundances almost two orders of magnitude lower than the grain surface formation route (see Fig. 7 to 9 and appendix 2 of Garrod et al. 2008).

At region 'F', little to no ice processing must have taken place due to the absence irradiation/heating at earlier stages, as opposed to the presence of a protostar at 'A' and 'B'. The young dynamical age of the NGC 2071 outflow (< 10⁴ yr, van Kempen et al., in prep) further corroborates this, limiting the production of CH₃CN.

6. Conclusions

This paper presented new data obtained with the SMA and Herschel-HIFI on the emission of organics around the cluster NGC 2071 and its outflow. The data were analyzed using a non-LTE radiative transfer code. The following conclusions are drawn:

- All organic emission detected by HIFI and the SMA observations originates in two or three regions, labelled 'A', 'B' and 'F'. 'A' and 'B' are the positions of the two central protostars, while 'F' is a shock position in the blue outflow. 'F' is spatially resolved in some lower excitation lines, but does not emit in CH₃CN.
- Using the non-LTE radiative transfer code RADEX, physical conditions of the three individual regions were constrained using a χ^2 analysis of the H₂CO and CH₃OH emission. Densities higher than 10^7 cm⁻³ (10^8 cm⁻³ in the case of 'B') and temperatures of 100 K or higher were derived.
- All HIFI CH₃OH detected are a sum of the emission of the three regions. On average 60-70% originates from 'B', 15-20% from 'A' and 15%-25% from 'F'. No line originates solely from either 'B' (the densest region) or 'A' (the hottest region).

- The high densities ($> 10^7$ cm⁻³) of the regions shield the gas-phase CH₃OH. Everywhere else, CH₃OH is destroyed through high-temperature reactions with hydrogen and/or through destructive sputtering.
- The significant difference between CH₃OH and H₂O line wing shapes and extent suggests H₂O formation through gas-phase synthesis along the flow.
- The lack of CH₃CN emission at 'F' is attributed to a difference in ice processing history.

Small-scale structure of organic emission is of vital importance in determining its origin and thus understand chemical processes during the early stages of star formations. Future observations with ALMA such as done in Jørgensen et al. (2013) are needed to determine if all organics emission lines originate from a shock-induced scenario or a hot corino. In the case of NGC 2071, the complexity of the chemistry could not be understood by single-dish observations alone.

Acknowledgements. The research of Tim van Kempen is made possible by the Allegro ARC node. Michel Fich, Carolyn M^cCoey and Sam Tisi are supported in this work by a Discovery Grant from NSERC and a Space Science Enhancement Program grant from the Canadian Space Agency. Doug Johnstone is supported by the National Research Council of Canada and by a Natural Sciences and Engineering Research Council of Canada (NSERC) Discovery Grant. We thank Mihkel Kama for useful discussions on methanol detections using HIFI. Michiel Hogerheijde and Floris van der Tak are thanked for assistance on RADEX. The WISH team, in particular Silvia Leurini, is thanked for useful discussions.

References

- Baulch, D. L. 2005, *Journal of Physical and Chemical Reference Data*, 34, 757
- Bisschop, S. E., Jørgensen, J. K., Bourke, T. L., Bottinelli, S., & van Dishoeck, E. F. 2008, *Astronomy and Astrophysics*, 488, 959
- Bottinelli, S., Ceccarelli, C., Lefloch, B., et al. 2004a, *The Astrophysical Journal*, 615, 354
- Bottinelli, S., Ceccarelli, C., Neri, R., et al. 2004b, *The Astrophysical Journal*, 617, L69
- Buckle, J. V. & Fuller, G. A. 2002, *Astronomy and Astrophysics*, 381, 77
- Butner, H. M., Evans, N. J. I., Harvey, P. M., et al. 1990, *Astrophysical Journal*, 364, 164
- Carrasco-González, C., Osorio, M., Anglada, G., et al. 2012, *The Astrophysical Journal*, 746, 71
- Caux, E., Kahane, C., Castets, A., et al. 2011, *Astronomy and Astrophysics*, 532, 23
- Cazaux, S., Tielens, A. G. G. M., Ceccarelli, C., et al. 2003, *The Astrophysical Journal*, 593, L51
- Ceccarelli, C., Caselli, P., Herbst, E., Tielens, A. G. G. M., & Caux, E. 2007, *Protostars and Planets V*, 47
- Chandler, C. J., Brogan, C. L., Shirley, Y. L., & Loinard, L. 2005, *The Astrophysical Journal*, 632, 371
- Comito, C., Schilke, P., Phillips, T. G., et al. 2005, *The Astrophysical Journal Supplement Series*, 156, 127
- de Graauw, T., Helmich, F. P., Phillips, T. G., et al. 2010, *Astronomy and Astrophysics*, 518, L6
- Flower, D. R. & Pineau Des Forêts, G. 2010, *Monthly Notices of the Royal Astronomical Society*, 406, 1745
- Garrod, R. T., Weaver, S. L. W., & Herbst, E. 2008, *The Astrophysical Journal*, 682, 283
- Johnstone, D., Boonman, A. M. S., & van Dishoeck, E. F. 2003, *Astronomy and Astrophysics*, 412, 157
- Jones, A. P., Tielens, A. G. G. M., & Hollenbach, D. J. 1996, *Astrophysical Journal* v.469, 469, 740
- Jørgensen, J. K., Bourke, T. L., Nguyen Luong, Q., & Takakuwa, S. 2011, *Astronomy and Astrophysics*, 534, A100
- Jørgensen, J. K., Favre, C., Bisschop, S. E., et al. 2012, *The Astrophysical Journal Letters*, 757, L4
- Jørgensen, J. K., Schöier, F. L., & van Dishoeck, E. F. 2002, *Astronomy and Astrophysics*, 389, 908
- Jørgensen, J. K., Visser, R., Sakai, N., et al. 2013, *The Astrophysical Journal Letters*, 779, L22
- Kama, M., Dominik, C., Maret, S., et al. 2010, *Astronomy and Astrophysics*, 521, L39

- Kama, M., López-Sepulcre, A., Dominik, C., et al. 2013, *Astronomy and Astrophysics*, 556, 57
- Kristensen, L. E., van Dishoeck, E. F., Benz, A. O., et al. 2013, *Astronomy and Astrophysics*, 557, 23
- Kristensen, L. E., van Dishoeck, E. F., Bergin, E. A., et al. 2012, *Astronomy and Astrophysics*, 542, 8
- Kristensen, L. E., Visser, R., van Dishoeck, E. F., et al. 2010, *Astronomy and Astrophysics*, 521, L30
- Kurtz, S., Cesaroni, R., Churchwell, E., Hofner, P., & Walmsley, C. M. 2000, *Protostars and Planets IV* (Book - Tucson: University of Arizona Press; eds Mannings, 299
- Laurini, S., Schilke, P., Wyrowski, F., & Menten, K. M. 2007, *Astronomy and Astrophysics*, 466, 215
- López-Sepulcre, A., Taquet, V., Sánchez-Monge, Á., et al. 2013, *Astronomy and Astrophysics*, 556, 62
- Maret, S., Ceccarelli, C., Tielens, A. G. G. M., et al. 2005, *Astronomy and Astrophysics*, 442, 527
- Öberg, K. I., Bottinelli, S., & van Dishoeck, E. F. 2009, *Astronomy and Astrophysics*, 494, L13
- Ott, S. 2010, in *Astronomical Data Analysis Software and Systems XIX. Proceedings of a conference held October 4-8, 139*
- Pilbratt, G. L., Riedinger, J. R., Passvogel, T., et al. 2010, *Astronomy and Astrophysics*, 518, L1
- Sandford, S. A. & Allamandola, L. J. 1993, *The Astrophysical Journal*, 417, 815
- Schöier, F. L., van der Tak, F. F. S., van Dishoeck, E. F., & Black, J. H. 2005, *Astronomy and Astrophysics*, 432, 369
- Scoville, N. Z., Sargent, A. I., Sanders, D. B., et al. 1986, *Astrophysical Journal*, 303, 416
- Shirley, Y. L., Evans, N. J. I., & Rawlings, J. M. C. 2002, *The Astrophysical Journal*, 575, 337
- Skinner, S. L., Sokal, K. R., Megeath, S. T., et al. 2009, *The Astrophysical Journal*, 701, 710
- Spaans, M., Hogerheijde, M. R., Mundy, L. G., & van Dishoeck, E. F. 1995, *Astrophysical Journal Letters* v.455, 455, L167
- Suutarinen, A. N., Kristensen, L. E., Mottram, J. C., Fraser, H. J., & van Dishoeck, E. F. 2014, *Monthly Notices of the Royal Astronomical Society*, 440, 1844
- Tafalla, M., Santiago-García, J., Hacar, A., & Bachiller, R. 2010, *Astronomy and Astrophysics*, 522, 91
- Takakuwa, S., Mikami, H., & Saito, M. 1998, *Astrophysical Journal* v.501, 501, 723
- Torrelles, J. M., Gómez, J. F., Rodríguez, L. F., et al. 1998, *The Astrophysical Journal*, 505, 756
- van der Tak, F. F. S., Black, J. H., Schöier, F. L., Jansen, D. J., & van Dishoeck, E. F. 2007, *Astronomy and Astrophysics*, 468, 627
- van der Tak, F. F. S., van Dishoeck, E. F., & Caselli, P. 2000, *Astronomy and Astrophysics*, 361, 327
- van Dishoeck, E. F., Blake, G. A., Jansen, D. J., & Groesbeck, T. D. 1995, *Astrophysical Journal* v.447, 447, 760
- van Dishoeck, E. F., Kristensen, L. E., Benz, A. O., et al. 2011, *Publications of the Astronomical Society of the Pacific*, 123, 138
- van Kempen, T. A., Longmore, S. N., Johnstone, D., Pillai, T., & Fuente, A. 2012, *The Astrophysical Journal*, 751, 137
- van Kempen, T. A., van Dishoeck, E. F., Güsten, R., et al. 2009, *Astronomy and Astrophysics*, 501, 633
- Visser, R., Kristensen, L. E., Bruderer, S., et al. 2012, *Astronomy and Astrophysics*, 537, 55